RESEARCH ARTICLE

Classification of Fog Life-Cycle Phases Using Ground-Based and Satellite-Based Observations

Maria Laura Pinilla[1,2,3] | **Eva Pauli**[2,3] | **Johannes Antenor Senn**[4] | **Jan Cermak**[2,3]

[1]Institute of Meteorology and Climate Research Troposphere Research, Karlsruhe Institute of Technology (KIT), Karlsruhe, Germany

[2]Institute of Meteorology and Climate Research Atmospheric Trace Gases and Remote Sensing, Karlsruhe Institute of Technology (KIT), Karlsruhe, Germany

[3]Institute of Photogrammetry and Remote Sensing, Karlsruhe Institute of Technology (KIT), Karlsruhe, Germany

[4]Institute of Geography and Geoecology, Karlsruhe Institute of Technology (KIT), Karlsruhe, Germany

Correspondence
Maria Laura Pinilla, Institute of Meteorology and Climate Research Troposphere Research, Karlsruhe Institute of Technology (KIT), Karlsruhe, Germany.
Email: maria-laura.pinilla@kit.edu

Abstract

A complete understanding of the fog life cycle—defined as formation, maturity, and dissipation phases—provides a basis for better predictions of fog formation and dissipation. While satellites can observe fog and low stratus (FLS) over a large spatial extent, ground-based instruments provide more detailed vertical and temporal information about fog at specific locations. In this study, we classify the life-cycle phases of radiation fog events during autumn 2009–2015 at a ground station in Southwest Germany by combining geostationary satellite observations with ceilometer and in situ measurements. For this, we develop a life-cycle phase classification algorithm that automatically detects the start and end times of each phase based on visibility trends and thresholds. Unlike other methodologies, we define fog life cycles not only through a visibility threshold of 1000 m but also by the processes involved during fog formation and dissipation. These processes are identified through changes in visibility trends and values and validated against backscatter patterns. Furthermore, we demonstrate that ground-based visibility detects radiation fog phases effectively, while its combination with ceilometer data has the potential to detect the life-cycle phases of cloud-base-lowering fog events. Thus, combining these data sources is essential for detecting the life-cycle phases of different fog types effectively. Finally, we find that ground-based data perform better in phase detection at individual locations compared with a satellite-based FLS life-cycle dataset.

KEYWORDS

Germany, fog, fog dissipation, fog formation, fog maturity, life cycles, low stratus, visibility

1 | INTRODUCTION

Fog is defined as tiny water droplets suspended in the atmosphere that lead to horizontal visibilities of < 1000 m at the Earth's surface (American Meteorological Society, 2024; World Meteorological Organization, 2017). An improved understanding of the fog life cycle allows better predictions of fog formation and dissipation. Low visibility conditions associated with fog modify radiation and thus alter the surface energy budget of the Earth

(Gultepe *et al.*, 2007; Vautard *et al.*, 2009). They represent a hazard to road, marine, and air transport worldwide (Gultepe *et al.*, 2007; Tardif & Rasmussen, 2007) and are a key element in predictions of photovoltaic power production (Köhler *et al.*, 2017). Fog combined with urban air pollution can have negative effects on human health (Pérez-Díaz *et al.*, 2017), but it serves as a water source for vegetation (Gottlieb *et al.*, 2019; Wang *et al.*, 2019), microbial communities (Warren-Rhodes *et al.*, 2013), fauna (Mitchell *et al.*, 2020) such as insects, for example, beetles (Seely, 1979), and human communities in arid ecosystems (Gultepe *et al.*, 2007). The main physical mechanisms of fog formation involve supersaturation produced by cooling, moistening, and/or mixing of air masses near the surface with different temperatures and the addition of water vapour to the air mass (Cotton *et al.*, 2011; Gultepe *et al.*, 2007). While fog can be classified based on its location (e.g., valley fog, mountain fog), it is typically classified into fog types (e.g., radiation, advection, cloud-base-lowering (CBL), precipitation, or evaporation fog) based on one or a combination of different formation mechanisms (Cotton *et al.*, 2011; Gultepe *et al.*, 2007; Pérez-Díaz *et al.*, 2017). In the following, we describe the formation mechanisms of the most relevant fog types for this study: radiation, advection, and CBL fog.

Radiation fog forms through nocturnal radiative cooling under clear skies (Cotton *et al.*, 2011; Gultepe *et al.*, 2007; Pérez-Díaz *et al.*, 2017; Price, 2019; Smith *et al.*, 2023; Tardif & Rasmussen, 2007). A temperature inversion forms in the air layer above the ground, which initiates cloud droplet activation and fog formation (Maalick *et al.*, 2016; Pérez-Díaz *et al.*, 2017). The ideal conditions for radiation fog formation are clear skies, a temperature inversion, wind speeds below about 2.5 m · s^{-1} associated with anticyclonic conditions, and high relative humidity (Cotton *et al.*, 2011; Gultepe *et al.*, 2007; Pérez-Díaz *et al.*, 2017; Tardif & Rasmussen, 2007). Radiation fog is one of the most prevalent fog types (Maalick *et al.*, 2016) and is most frequent in central Europe (Gultepe *et al.*, 2007), particularly in autumn, when nights are humid and sufficiently long for temperatures to decrease significantly (Maalick *et al.*, 2016; Pérez-Díaz *et al.*, 2017; Román-Cascón *et al.*, 2019). While radiation fog forms under stable conditions, advection fog formation occurs by the movement of warm, moist air over a cold surface, which leads to condensation due to the cooling of the air layer closest to the cold surface (Pérez-Díaz *et al.*, 2017; Smith *et al.*, 2023). Constant winds greater than 2.5 m · s^{-1} are necessary to form advection fog (Tardif & Rasmussen, 2007). The lowering of the base of low stratus clouds all the way to the surface to form fog

is known as CBL fog (Gultepe *et al.*, 2007; Román-Cascón *et al.*, 2019). It is related to radiative cooling at the cloud top, generating downward turbulent mixing, which cools the sub-cloud layer and lowers the cloud base (Gultepe *et al.*, 2007; Tardif & Rasmussen, 2007).

In contrast to fog formation, fog dissipation does not depend on the type of fog. Fog dissipates primarily after sunrise, as incoming solar radiation increases the near-surface sensible heat flux, leading to a burn-off of the fog layer (Dione *et al.*, 2023; Maalick *et al.*, 2016; Pérez-Díaz *et al.*, 2017; Román-Cascón *et al.*, 2019). Near-surface wind speeds of around 2–3 m · s^{-1} are also favourable (Dupont *et al.*, 2012) for fog dissipation. If the fog layer has grown high enough during the night, dissipation starts at the surface and the fog transforms into a low stratus cloud, which can persist for the whole day (Maalick *et al.*, 2016; Román-Cascón *et al.*, 2019). If the cloud layer does not dissipate completely over the course of the day, it can then be the starting point for a CBL event, leading to subsequent fog events over multiple days (Román-Cascón *et al.*, 2019).

Fog can be observed from the satellite and the ground perspective. From the satellite perspective, fog can be observed as a cloud touching the ground (Cermak & Bendix, 2011; Lamb & Verlinde, 2011) and is usually studied collectively with low stratus (fog and low stratus, hereafter FLS), since the separation of these two phenomena is technically challenging and irrelevant for a number of applications (Cermak, 2018; Cermak & Bendix, 2011; Egli *et al.*, 2017). FLS detection schemes provide high-resolution spatial and temporal information on FLS occurrence (Cermak, 2006; Cermak & Bendix, 2007, 2008; Egli *et al.*, 2017; Jahani *et al.*, 2025) and life cycle (Pauli *et al.*, 2022a). Additionally, vertical distributions of FLS have been studied using active satellite-based sensors in Cermak (2018), Pauli *et al.* (2022b), and Qiao *et al.* (2022). Furthermore, satellite-based FLS datasets have previously been used to understand and predict spatial and seasonal patterns of FLS occurrence and formation and dissipation times on large spatial and temporal scales (Egli *et al.*, 2017; Pauli *et al.*, 2020; Pauli *et al.*, 2022a; Pauli *et al.*, 2024a, 2024b).

While satellite data can provide information on large areas and have great potential for automation, ground-based measurements provide higher accuracy and higher temporal resolution. Ground-based remote sensing instruments such as ceilometers and in situ sensors offer detailed information about fog at these locations, including cloud-base height (CBH), cloud-top height (CTH), horizontal and vertical visibility, and vertical profiles of thermodynamic variables (Dupont *et al.*, 2012). They allow the identification of fog occurrence

(Tardif & Rasmussen, 2007), can be used as ground-truth data for the separation of fog from low stratus (Qiao *et al.*, 2022), and can be used to explain the development of the different fog life-cycle phases (Dione *et al.*, 2023; Dupont *et al.*, 2012; Toledo *et al.*, 2021). In this article, the term FLS is used when referring to fog from the satellite perspective and the terms fog or low stratus are used in events where the ground-based observations allow this separation.

Life-cycle phases have been defined and detected from the ground and from the satellite perspective in many studies. From the satellite perspective, Pauli *et al.* (2022a) detected the formation and dissipation times of FLS events by applying logistic regression to a 10-year FLS dataset over central Europe. From the ground perspective, three or more phases have been detected based on, for example, turbulent kinetic energy (Nakanishi, 2000), a double-sum curve analysis (Maier *et al.*, 2013), or the evolution of visibility and microphysical parameters (Dione *et al.*, 2023; Mazoyer *et al.*, 2022; Toledo *et al.*, 2021; Weston *et al.*, 2022). Although these studies have defined different life-cycle times and phases, the beginning and end of the phases either are not clearly detected or are set to a predefined temporal window (30–90 minutes) before and after the detected formation and dissipation times (Dione *et al.*, 2023; Toledo *et al.*, 2021), which makes the phase detection unspecific to the fog situations and life-cycle processes. Other definitions require large eddy simulation models (Nakanishi, 2000) or do not provide phase definitions (Pauli *et al.*, 2022a). Moreover, to our knowledge, a comparison of the two observational perspectives (i.e., satellite versus ground-based) regarding fog life-cycle phase detection has not been conducted.

Therefore, the goal of this study is to detect, classify, and characterize the fog life-cycle phases based on fog formation and dissipation mechanisms. We define three life-cycle phases in this study: formation, maturity, and dissipation, and detect the phases by defining visibility and visibility trend thresholds. These phases are characterized further based on the development of temperature, relative humidity, visibility, and wind speed. Moreover, we compare the development of the phases in the ceilometer profiles with the satellite-based FLS detection to find the features that can be detected with each instrument and to evaluate the possibilities of detecting the phases solely from the backscatter profiles or the satellite data. This study addresses two main research questions. (a) How can fog life-cycle phases be detected automatically using a combination of satellite and ground-based observations? (b) What are the characteristics of surface variables during these phases?

2 | DATA AND METHODS

2.1 | Data

The study site is the German Weather Service (Deutscher Wetterdienst, DWD) weather station in Rheinstetten (48.97°N, 8.33°E, 116.10 m above sea height level), located in the Upper Rhine Valley in Southwest Germany (Figure 1a). At the site, radiation fog predominates, especially in the colder months (Egli *et al.*, 2017; Bendix, 2002; Pauli *et al.*, 2022a), leading to maximum fog occurrence in autumn, followed by winter, and a minimum in summer (Figure 1c). In the region, fog mainly forms due to condensation processes after sunset or at night, given by cold-air drainage flow from the surrounding areas (Egli *et al.*, 2017), and dissipates in the morning or midday hours (Pauli *et al.*, 2022a). FLS occurrence, from the satellite perspective, is on average between 5 and 6 hours per day in autumn and winter (Figure 1b).

The satellite dataset used in this study is the FLS dataset by Egli *et al.* (2017), derived from the geostationary *Meteosat Second Generation* satellites and scanned by the Spinning Enhanced Visible and InfraRed Imager (SEVIRI) with a 15-minute temporal resolution and ≈ 5-km spatial resolution over Europe. This binary FLS product (FLS present = 1, FLS not present = 0) is based on the satellite-based operational fog observation scheme (SOFOS) by Cermak (2006) (later adapted by Cermak & Bendix, 2007, 2008, and Egli *et al.*, 2017), which separates FLS from clear sky and other clouds by applying a combination of spectral (e.g., cloud-free areas, ice and snow pixels) and spatial (e.g., altitude and surface homogeneity) tests. FLS formation and dissipation times are obtained from Pauli *et al.* (2022a), and are derived by applying logistic regression to the FLS time series from Egli *et al.* (2017). Both datasets cover the European continent from 2006 to 2015.

We use ceilometer and surface observations from the DWD weather station Rheinstetten between 2009 and 2015 to obtain information on ground-fog presence, fog vertical extent, and fog surface conditions. Since the ceilometer data at the study site are available from 2009, we set the study period to 2009–2015. The ceilometer at the study site (type CHM15K, from the DWD's ceilometer network: Deutscher Wetter Dienst., 2021) measures atmospheric backscatter up to 15,000 m above ground level (m agl) and reports the measurements as temporal averages every 15 seconds. It uses the 1064-nm wavelength for vertical atmospheric profiling with the Light Detection and Ranging (lidar) technique (Lufft., 2025). The measured backscatter signal is processed by the data providers and distributed as a normalized range-corrected
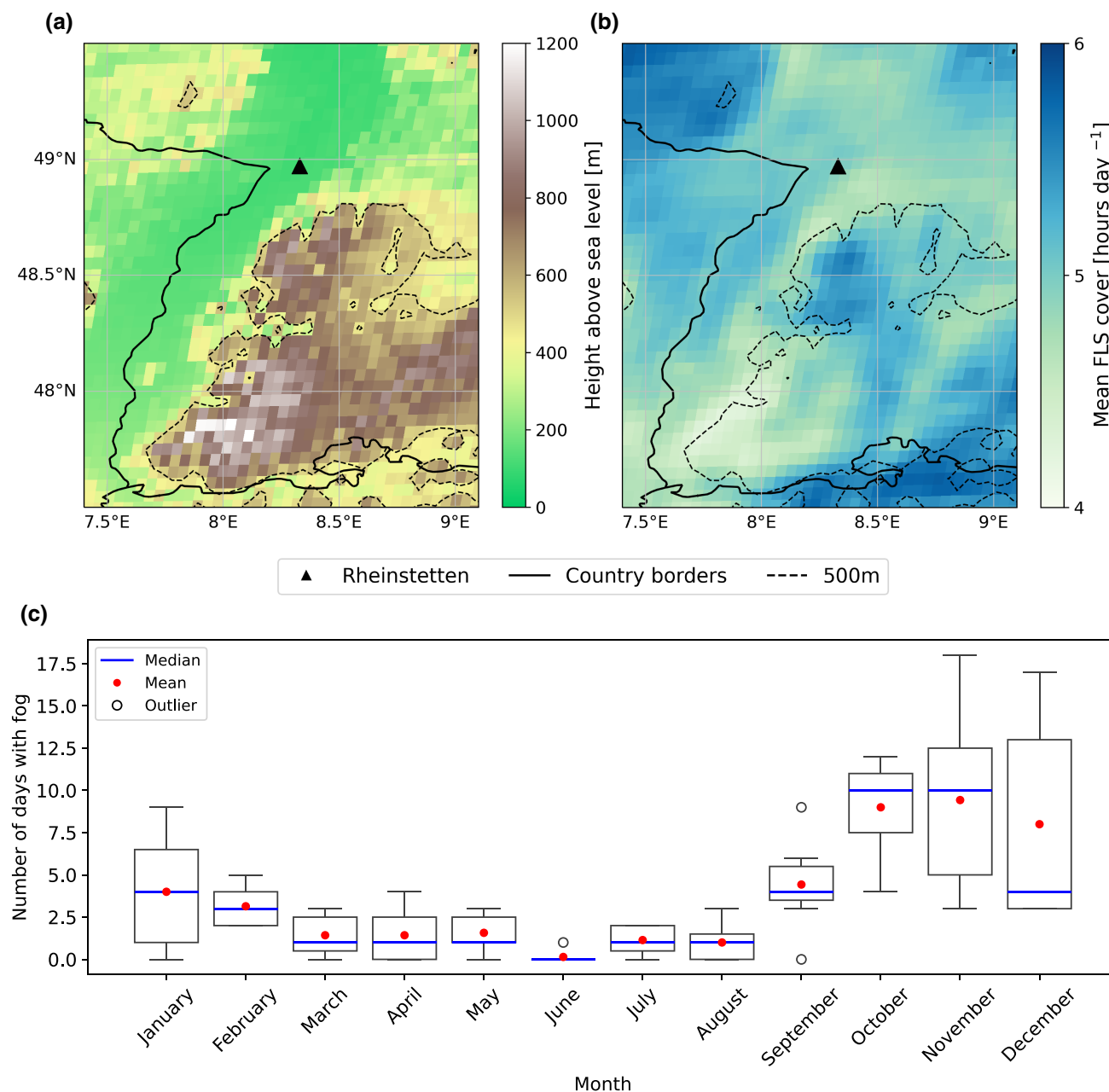
FIGURE 1 (a) Mean height above sea level in metres (Digital Elevation Model by Hijmans *et al.*, 2005). (b) Mean fog and low stratus (FLS) cover for autumn and winter 2009–2015 in hours per day in Southwest Germany (dataset by Egli *et al.*, 2017). A black triangle denotes the German Weather Service (DWD) weather station in Rheinstetten. The black lines represent country borders and also mark the course of the Rhine River from approximately 47.5–49°N. The dashed black line represents a height of 500 m above sea level. Panels (a) and (b) were adapted to the study site from Pauli *et al.* (2022a). (c) Monthly distribution of the number of days with fog occurrence in the study area for 2009–2016 with observations from the DWD station in Rheinstetten. [Colour figure can be viewed at wileyonlinelibrary.com]

signal (Mattis & Wagner, 2014). Additionally, the DWD meteorological station at the study site provides data on air temperature and relative humidity at 2 m agl, horizontal visibility at 2.5 m agl and wind speed at 10 m agl with a one-hour temporal resolution, as well as days with fog occurrence generated from SYNOP reports. The instruments used at the DWD weather station can be found in the Supporting Information Table S1.

2.2 | Methods

2.2.1 | FLS event selection

We select FLS events from October and February 2009–2015 to represent the two seasons with the most frequent FLS occurrence. These months are selected because they are the two months with the most clear-sky days

available from the datasets, and clear-sky conditions serve as a proxy for radiation fog formation. For the selection of single events, we follow the steps below.

1. First, we choose fog events which either start or end in clear-sky conditions. Clear-sky scenes over Rheinstetten are selected from the National Aeronautics and Space Administration (NASA) Worldview using the corrected reflectance (True Color) base layer based on *Terra*/Moderate Resolution Imaging Spectroradiometer (MODIS) data.
2. For those clear-sky days, days with observed FLS and FLS life-cycle times from the satellite-based datasets at the Rheinstetten pixel are selected. If formation and dissipation times are not available for this pixel, these times are selected from the nearest pixel with available times inside an area of 3×3 pixels centred at the Rheinstetten pixel ($\pm 0.065°$ longitude and latitude).
3. We set a minimum event duration of three hours to obtain at least three measurements with one-hourly resolution for each event, as this is required for a successful application of our fog life-cycle classification scheme. Therefore, if formation and dissipation times are available and the difference between them is at least three hours, the FLS event is selected.
4. The list of FLS events is updated based on ceilometer data availability.
5. Finally, the FLS events are classified as *fog* or *low stratus*, observing the ceilometer backscatter profiles and the station fog occurrence data. High backscatter signals that begin from the ground ("touch the ground") in the ceilometer profiles indicate that FLS observed from the satellite perspective is a fog situation. In contrast, high backscatter signals that begin above the ground indicate that FLS is a low stratus situation. Additionally, the fog classification is validated with fog occurrence data from the station.

The final selection includes a total of 21 FLS events (15 events in October and six in February). Among them, fog is detected in seven events (all of them in October) and low stratus in 14 events. The formation and dissipation times are selected from the Rheinstetten pixel for 11 events and from the surrounding pixels for 10 events.

2.2.2 | Fog-type classification

The detected fog events are then classified into fog types following the fog-type classification algorithm from Tardif and Rasmussen (2007). For this purpose, the surface conditions of wind speed, cloudiness, and temperature one hour before fog formation extracted from the Pauli

et al. (2022a) dataset are analyzed as described in Figure 2. The wind-speed threshold is the main factor in separating advection processes (e.g., advection fog) from local-scale turbulence features (e.g., radiation fog), which should be adapted to the study site conditions (Guerreiro *et al.*, 2020). For this purpose, the mean wind-speed values are calculated within a time range of 10 hours before and after each event's formation and dissipation, respectively, obtaining a mean value of $2.5 \, \mathrm{m \cdot s^{-1}}$. A wind-speed value of $2.5 \, \mathrm{m \cdot s^{-1}}$ is then selected as the threshold value that represents the separation between high and low wind speeds around FLS events at the study site. Information on clear skies and CBH is obtained from the ground perspective using the ceilometer profiles, which allows the identification of possible cloud-base-lowering situations. Cooling, as an indicator for radiation fog formation, is evaluated using the time-series data from the station. Using this adapted algorithm, the advection, radiation, and CBL fog types can be identified. If none of the criteria is fulfilled, the fog event is classified as *unknown*.

2.2.3 | Fog formation, maturity, and dissipation time detection

In the next step, the life-cycle phases of the radiation fog events are detected from the ground perspective using visibility data. This detection is focused on radiation fog, since it is the predominant fog type observed. The selected events are evaluated in the algorithm starting 10 hours before formation time from the FLS life-cycle dataset (Pauli *et al.*, 2022a). The algorithm then evaluates each time step of the time series, analyzing the visibility trend, the actual visibility value, and/or the visibilities in the following hours, as described in Figures 3 and 4. In Figure 3, the time blocks implemented in the life-cycle time classification algorithm are illustrated: blue exemplifies the visibility rolling mean formed by three consecutive time steps, red the visibility values of the time steps in the next hour, and orange the visibility trends or values of the time steps in the next three hours after the time step that is currently being evaluated by the algorithm. The hourly visibility observations are resampled to a 15-minute resolution by applying a linear interpolation of the values, assuming a linear behaviour of the visibilities between the actual observations. This is done as visibilities may change drastically within two consecutive hours, that is, from 600 to 20,000 m. Hence, this approach allows a better assessment of the visibilities and a more accurate approximation of the life-cycle times detected.

The analysis of visibility thresholds and trends enables the detection of the time when fog formation begins and ends (formation phase), when the fog is fully
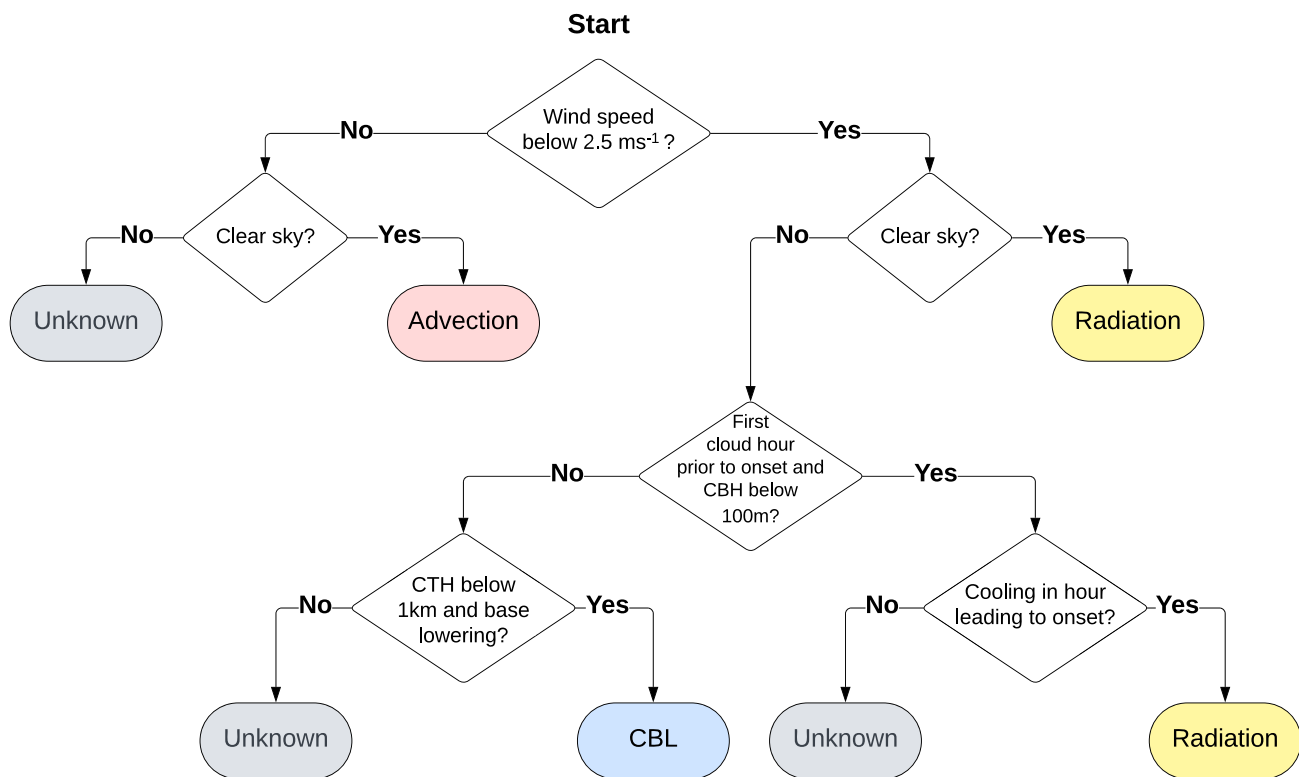
FIGURE 2 Fog-type classification algorithm adapted from Tardif and Rasmussen (2007) and Guerreiro *et al.* (2020). Each decision step should be evaluated one hour before fog and low stratus (FLS) formation, that is, onset. The fog types that can be classified with this adapted workflow are advection, radiation, and cloud-base-lowering (CBL) fog. If none of the physical conditions before the fog event matches with any of the classification steps, the fog type is classified as *unknown*. [Colour figure can be viewed at wileyonlinelibrary.com]
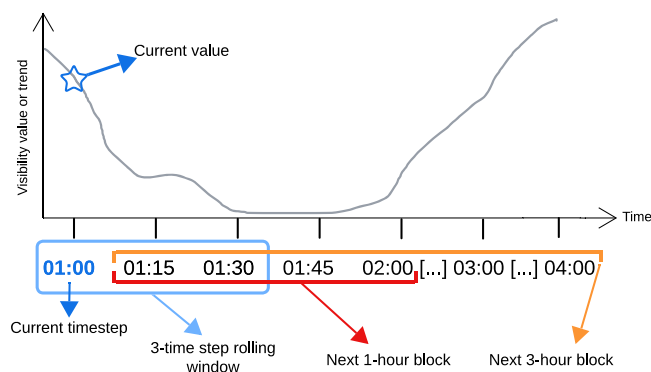

FIGURE 3 Description of the time blocks implemented in the life-cycle times classification algorithm. Blue exemplifies the visibility rolling mean, red the visibility values in the next hour, and orange the visibility trends or values in the next three hours. [Colour figure can be viewed at wileyonlinelibrary.com]

(American Meteorological Society, 2024; World Meteorological Organization, 2017). The second one, 5000 m, follows the definition of mist, as in Román-Cascón *et al.* (2019), and is used in this study as a proxy for the distinction between low and high visibilities. Additionally, we calculate the visibility differences between each consecutive observation to analyze the visibility trends. Then, the rolling mean values of these differences are calculated inside a window of three consecutive time steps to observe how the average of the visibility differences changes across time. The visibility trend is mostly negative before fog onset, close to zero during fog presence, that is, visibility under 1000 m, and primarily positive after fog occurrence.

The algorithm is designed to identify the phases in chronological order: formation, maturity, and dissipation. For a subsequent phase to be detected, the preceding phase must be detected first. For example, if the formation phase has not been detected, the maturity and dissipation phases cannot be detected yet. Figure 4 describes the different labels that are assigned in the algorithm. The labels are indicated by numbers in brackets, from 1 to 9, in the coloured ovals at the end of each process (i.e., flow chart terminators). At the first decision step, the algorithm detects a negative visibility trend in the current time step

formed (maturity phase), and when fog dissipation starts and ends (dissipation phase). A progressive decrease (increase) in visibility serves as a proxy for the beginning of fog formation (dissipation). Two visibility thresholds are included in the algorithm. The first one, 1000 m, follows the international definition of fog occurrence

Start

Visibility trend in current timestep

- < 0 | 0 → **Formation phase** → Visibility trends in the next 3 hours
- < 0 | 0 | > 0 & formation detected → **Maturity phase** → Visibilities in the next hour < 1000 m
- > 0 & maturity detected → **Dissipation phase** → **All** visibilities in the next 3 hours > 1000 m

Formation phase:
- 1 or more > 0 → Formation not started (1)
- all < 0 → Formation starts (2)
- all < 0 & formation detected → Formation continues (3)

Maturity phase:
- **all** & current visibility < 1000 m → Maturity starts (4)
- **1 or more** & maturity detcted → Maturity continues (5)

Dissipation phase:
- current visibility < 5000 m → Dissipation starts (6)
- current visibility < 5000 m & dissipation detected → Dissipation continues (7)
- current visibility > 5000 m → Dissipation ends (8)
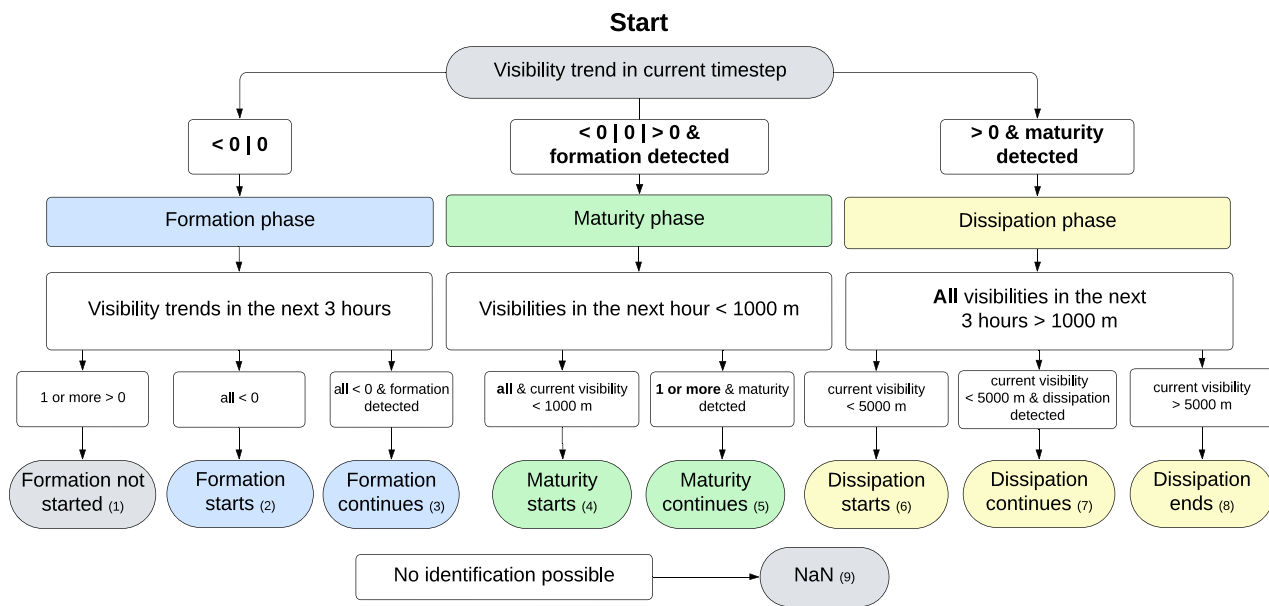
No identification possible → NaN (9)

FIGURE 4 Workflow of the life-cycle time classification algorithm based on visibility data. [Colour figure can be viewed at wileyonlinelibrary.com]

as the possible beginning of fog formation. If a positive visibility trend is present in the following three hours, the formation phase has not yet started (label 1). In contrast, negative trends during the next three hours mean the start of formation (label 2) or, if formation has already been identified, the continuation of this phase (label 3). After formation has been detected, visibilities below 1000 m at the current time step and during the following hour detect the beginning of the maturity phase and the end of the formation phase (label 4). After that, at least one time step with visibility below 1000 m during the following hour indicates the continuation of the maturity phase (label 5). A positive visibility trend and visibilities above the 1000-m threshold in the consecutive three hours set the start of the dissipation phase and the end of the maturity phase (label 6). If the visibilities remain under the 5000-m threshold, the dissipation phase continues (label 7). Dissipation ends when the current visibility and all visibility values in the next three hours surpass the 5000-m threshold (label 8). If the values of the current time step do not match any of the described labels, the time step is considered part of the phase assigned to the previous time step. The algorithm stops when the end time of the dissipation phase is identified.

3 | RESULTS AND DISCUSSION

In general, fog events are observed in October and low stratus events are observed in February (cf. Table S2). Most of the events show an overall good agreement between the

times at which FLS is identified from the satellite perspective and those from the ceilometer, which is the case for the events in both case studies that are presented in the following subsection. Five fog events are classified as radiation fog, one as CBL fog, and one cannot be classified into any fog type due to insufficient data availability (cf. Table S2). The radiation fog events (cf. Table S3) follow a classic radiation fog pathway, with formation in the evening or at night driven by radiative cooling. The maturity phase is always reached at night and dissipation begins at or shortly after sunrise, most likely due to surface warming induced by solar radiation. In the following (Sections 3.1 and 3.2), we present two radiation and one CBL fog event.

3.1 | Case study 1: Radiation fog event in October 2014

A radiation fog event that begins on the evening of October 18, 2014 and ends the following morning of October 19, 2014 is shown in Figure 5. The vertical fog layer observed in the ceilometer profile (in dark red) extends up to 100 m agl, and at roughly the same time the satellite-based FLS mask indicates FLS occurrence.

3.1.1 | Fog formation

According to the visibility-based life-cycle times, the formation phase begins on the first day at 1845 (UTC+2) and ends on the second day at 0200. During this phase,
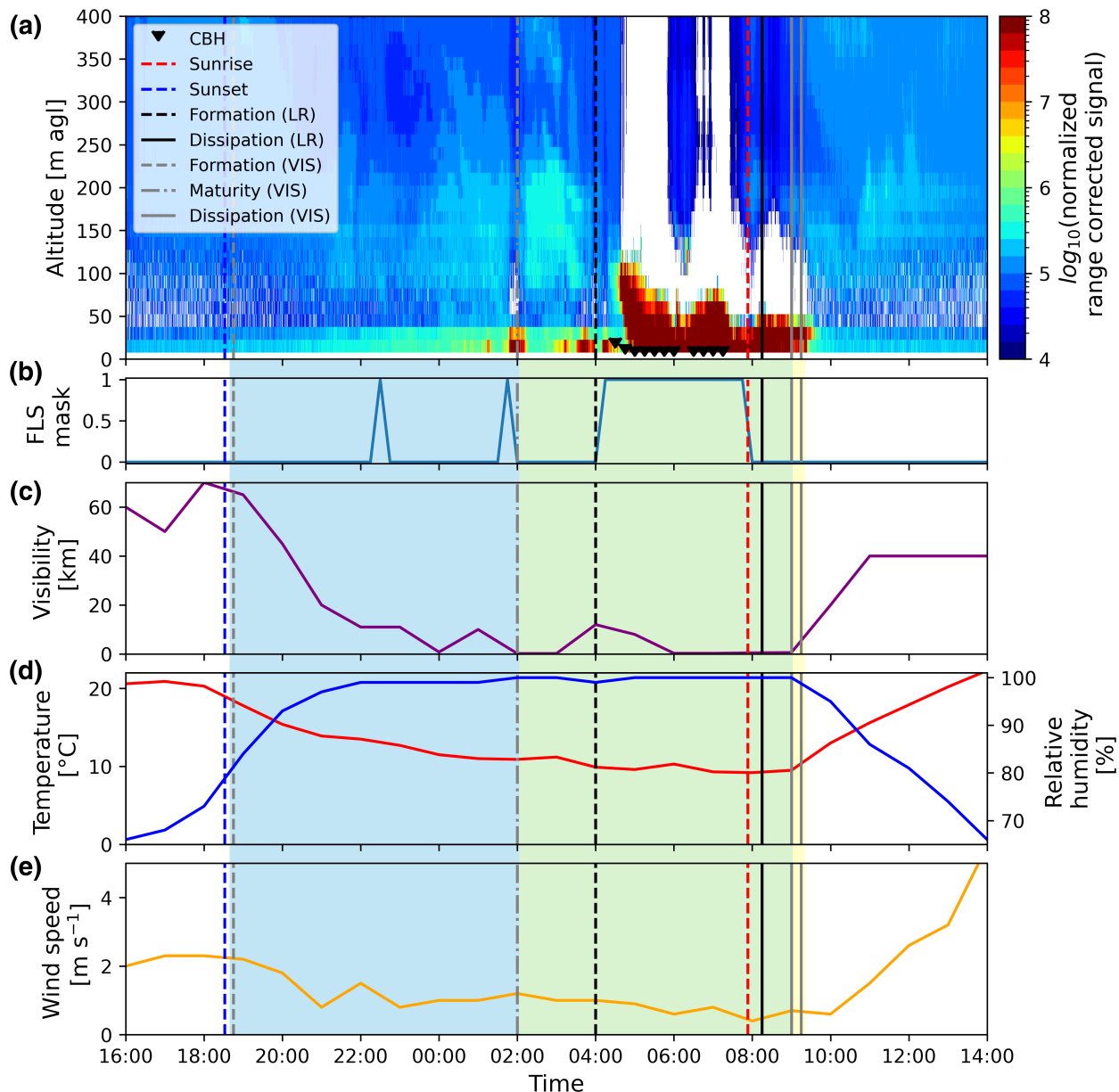
FIGURE 5   Radiation fog event (event ID 11) from October 18–19, 2014 (UTC+2) at the station Rheinstetten. (a) Vertical profile of normalized range-corrected signal on a logarithmic scale from 0 to 600 m agl. Fog is coloured dark red below 200 m agl. (b) Fog and low stratus (FLS) binary mask (FLS present=1, FLS not present=0). (c) Visibility (1 km close to the *x*-axis line and 5 km at the intersection with the dissipation end line). (d) Air temperature (in red) and relative humidity (in blue). (e) Wind speed. Vertical dashed red and blue lines represent the sunrise and sunset times, respectively. Vertical grey lines denote the calculated life-cycle times based on visibility (VIS in the legend): formation start (dashed), maturity start (dot–dashed), and dissipation start and end (solid lines). The three corresponding phases are highlighted with coloured backgrounds from (b)–(d): formation in blue, maturity in green, and dissipation in yellow. Vertical black lines denote the formation time (dashed) and the dissipation time (solid lines) based on the satellite-based linear regression (LR in the legend) approach from Pauli *et al.* (2022a). Black triangles represent the cloud-base height (CBH). [Colour figure can be viewed at wileyonlinelibrary.com]

fog develops slowly, indicated by an increasing backscatter signal in the ceilometer profile and visibility fluctuations from midnight onwards. In the last hour of the formation phase, the fog has a vertical extent below 50 m agl. The surface conditions, described by visibility, temperature, relative humidity, and wind speed, show distinct features

during this fog event (cf. Figure 5c–e). A constant decrease in visibility characterizes this phase. The temperature decreases to 10°C, caused by radiative cooling, while the relative humidity increases to 100%, leading to air saturation and ideal conditions for radiation fog formation (Cotton *et al.*, 2011). Wind speed during formation is

low (around 0.5–$1\,\mathrm{m}\cdot\mathrm{s}^{-1}$) and therefore ideal for radiation fog formation (Pérez-Díaz *et al.*, 2017; Tardif & Rasmussen, 2007).

An inverse correlation can be seen between air temperature and relative humidity. This is an expected relationship, described by the dependence of the saturation water vapour on temperature in the Clausius–Clapeyron equation (Lamb & Verlinde, 2011). Since warm air can take up more water vapour than colder air, a decrease in the air temperature leads to a higher relative humidity and vice versa. Another inverse correlation is observed between visibility and relative humidity. The relative humidity, as an indicator of water-vapour saturation in the air, can be a proxy for visibility due to the scattering of suspended water droplets. This correlation is, however, not always present at the formation phase. For example, the visibility may decrease before and during formation, while the relative humidity stays at the same value or already indicates saturation before the visibility decreases. A possible explanation is that, although the air is saturated hours before the visibility falls below 1000 m, the droplet formation starts later due to less aerosol load compared with days where visibility and relative humidity correlate during formation. Considering the role of aerosols as cloud condensation nuclei and their strong influence on droplet concentrations and sizes, aerosol activation is critical for fog formation and development (Maalick *et al.*, 2016; Pauli *et al.*, 2024b). To confirm this hypothesis, further studies should include measurements of aerosols and microphysical parameters (i.e., fog-droplet number concentration). Analyses of the boundary-layer height would also provide information on the aerosol-layer concentration at the study site.

3.1.2 | Fog maturity

The maturity phase begins at 0200 and ends at 0900, represented by visibilities under 1000 m for at least three consecutive time steps at the beginning of the phase and an increase of the backscatter signal. The minimum visibility reached during maturity is 200 m, which is similar to radiation fog events near Paris in Weston *et al.* (2022) and Dione *et al.* (2023). It increases slightly during the last two hours of the maturity phase (from 300 to 600 m), similar to the observations in Mazoyer *et al.* (2022). While visibility generally remains under 1000 m, it can fluctuate, reaching values above this threshold at different time steps during the first half of the phase. Constant values of surface conditions that are usually reached at the end of formation characterize the maturity phase. While the air temperature can decrease during maturity, relative humidity remains

at saturation and wind speeds remain constant (Dione *et al.*, 2023; Weston *et al.*, 2022).

3.1.3 | Fog dissipation

The dissipation phase begins at 0900 and ends 15 minutes later. The satellite-based FLS mask indicates no FLS presence already one hour before dissipation starts, likely due to the inability to detect FLS during sunrise. The visibility and air temperature increase almost linearly and continue to do so after this phase. This increase does not occur directly after sunrise but about one hour later, as the solar radiation does not reach the surface until the fog layer starts to dissipate. The relative humidity decreases following a similar but inverse behaviour to the visibility and the temperature. The wind speed increases after fog dissipation from $\approx 0.5\,\mathrm{m}\cdot\mathrm{s}^{-1}$ to values above $2.5\,\mathrm{m}\cdot\mathrm{s}^{-1}$ two hours later, likely due to turbulent heat fluxes induced by solar warming (Dupont *et al.*, 2016). The dissipation phase is characterized by faster changes than those in the formation phase and is the shortest phase compared with formation and maturity, surpassing the visibility threshold of 5000 m within 15 minutes. A rapid increase in visibility during this phase has also been observed by Toledo *et al.* (2021) and Mazoyer *et al.* (2022) during fog dissipation.

3.2 | Case study 2: Radiation fog and CBL fog events in October 2015

A long event of both fog and low stratus, which persists for three consecutive days, is shown in Figure 6. It consists of a radiation fog event (on the left) that begins on the evening of October 26, 2015, transitions into a low stratus by base lifting at noon on October 27, 2015 and lowers its base again at midnight of October 28, 2015, resulting in a CBL fog event (on the right) that persists until noon. In total, it has a duration of ≈ 40 hours, which is the longest FLS event observed in this study.

The FLS mask detects the first FLS presence at the same time when fog is observed for the first time in the ceilometer profile. The FLS mask indicates FLS presence with a signal that alternates between 0 and 1 until the middle of the CBL fog event. The visibility-based life-cycle times are only detected for the radiation fog event (first fog event), which is explained in the following subsections. This case study represents this study's most persistent and developed fog event. Both the lifting and the lowering of the base are well shown by the CBH data between the ground height and ≈ 200 m agl.
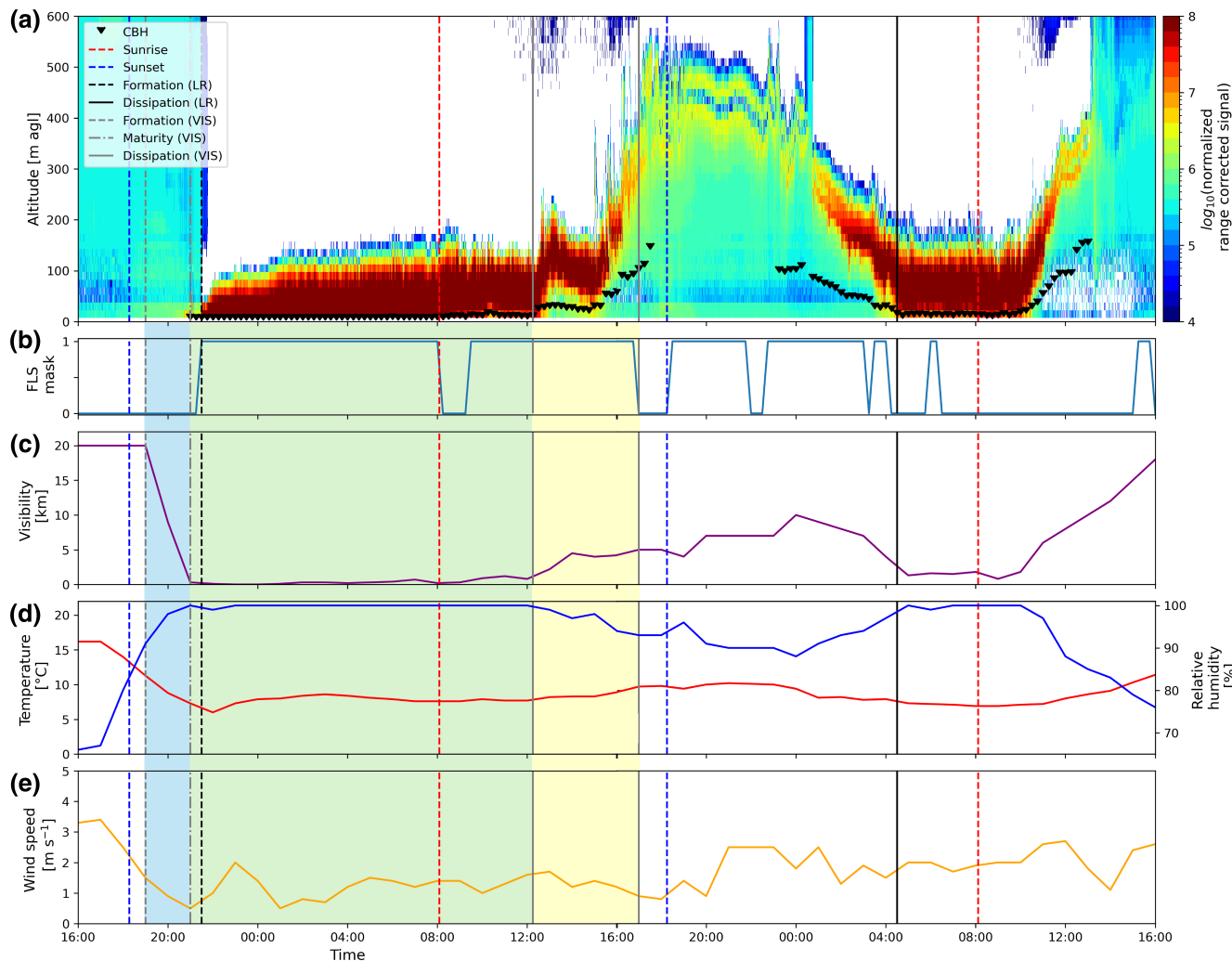
FIGURE 6 (Left) A radiation fog event (ID 13) from October 26–27, 2015 (UTC+2) that develops into (right) a cloud-base-lowering (CBL) fog event (ID 14) from October 27–28, 2015 (both local time) at the station Rheinstetten. Further description as in Figure 5. [Colour figure can be viewed at wileyonlinelibrary.com]

3.2.1 | Fog formation

The formation phase starts at 1900 and ends two hours later. During this period, the backscatter signal above ground increases its intensity slightly. The surface conditions are shown in Figure 5c–e. The visibility decreases abruptly during the visibility-based formation phase to values below the 1000-m threshold. Meanwhile, the air temperature drops from 12 °C to 7°C due to longwave radiative cooling and the relative humidity increases rapidly (from approximately 70% at 1700) before the formation phase on the first day, reaching saturation (100%) at the end of the phase. In this case study, the visibility and temperature also show an inverse correlation with the relative humidity during the radiation fog event, as in case study 1. Before and during the fog formation phase, the wind speed decreases linearly from values higher than 3.0 m·s^{-1} to 0.5 m·s^{-1}, probably as a result of

near-surface air cooling around sunset. A reduction in wind speed keeps the moisture in the lower atmosphere, preventing its deposition as dew at the surface, therefore providing sufficient moisture for fog formation when the temperature decreases as a result of radiative cooling (Cotton *et al.*, 2011).

3.2.2 | Fog maturity

This phase begins with a formed fog layer with a visibility of 300 m that decreases to zero in the middle of the maturity phase. The fog layer slowly increases its vertical extent up to 100 m agl from the middle of maturity to its end. The CBH also follows a similar pattern, starting from ≈ 4 m agl and ending at ≈ 55 m agl. Fog persists for ≈ 16 hours. The air temperature and relative humidity both remain relatively constant (8°C and 100% respectively),

while the wind speed varies from $2\,m\cdot s^{-1}$ to around $1\,m\cdot s^{-1}$ during the phase. The mature radiation fog layer in case study 2 has a higher vertical extent (≈ 100 vs. below $100\,m$), is thicker (minimum visibility 0 versus $200\,m$), and lasts longer (≈ 15 vs. 7 hours) than in case study 1. These characteristics can indicate how developed each event is (Price, 2011, 2019). Deep adiabatic fog layers often reach $100\,m$ depth or more (Dione *et al.*, 2023; Price, 2011), are optically thicker, and are usually more persistent (can last 24 hours or more), while shallow fog layers are usually less than $100\,m$ deep, optically thinner, and short-lived (less than 8–10 hours: Price, 2011, 2019). In addition, thicker fog layers are more likely to transition into low stratus, which reinforces a slow increase in solar downwelling flux and, consequently, a slow increase in temperature, as observed in case study 2 (Dupont *et al.*, 2016). The wind speed during radiation fog in case study 2, on average, is higher and more variable than in case study 1. Stronger wind speeds promote more turbulence within the fog layer, affecting the evolution from shallow fog to deep adiabatic fog (Smith *et al.*, 2018). In this sense, we can define the radiation fog in case study 2 as a deep adiabatic radiation fog and that in case study 1 as shallow fog.

3.2.3 | Fog dissipation/cloud-base lifting

Radiation fog dissipation starts at 1215, indicated by an increase in CBH to a height of $500\,m$ agl and an increase in visibility surpassing the 1000-m threshold. The temperature increases only slightly by $2°C$, as there is only a slow increase in the downwelling solar radiation due to the persistent lifted stratus layer. Both the relative humidity and the wind speed decrease slowly during the dissipation phase (to 93% and $\approx 1\,m\cdot s^{-1}$, respectively). Therefore, the fog water mass is not depleted as in case study 1 but elevated into a low stratus layer. Dissipation in case study 2 is therefore quite different from that in case study 1: the dissipation phase in case study 2 is driven by stratus lifting, lasts longer (≈ 5 hours), and starts later (around noon) compared with case study 1 (15-minute duration starting in the morning). These differences, as in the maturity phase, can be related to the differences between shallow versus deep adiabatic fog. While shallow fogs usually dissipate during the morning, as the solar-induced sensible heat fluxes generate sufficient energy for the dissipation of the fog layer, deep fog is more persistent and therefore dissipates later, and more likely transitions into a low stratus cloud (Dupont *et al.*, 2016; Price, 2019). Therefore, the dissipation of the fog event in case study 2 occurs through cloud-base lifting, which can be explained by the thickness and relatively high vertical extension of the fog layer, which impede dissipation due to solar radiation warming

(Maalick *et al.*, 2016), or by a deficit in the liquid water path contained in the fog layer (Toledo *et al.*, 2021; Wærsted *et al.*, 2019).

3.2.4 | Cloud-base lowering

The top of the lifted cloud reaches a maximum height of $500\,m$ agl around 2000, and starts to lower again at 2300. The visibility stops increasing and starts to decrease from $\approx 10\,km$ to 1000–2000 m and the wind speed fluctuates at values favourable for cloud-base lowering (0.5 and $2.5\,m\cdot s^{-1}$: Toledo *et al.*, 2021). The air temperature decreases slightly to $\approx 7°C$, whereas the relative humidity shows a more pronounced increase to saturation, showing in this case a less pronounced correlation of relative humidity and temperature compared with the radiation fog formation phase at the beginning of the event. The weak temperature decrease and consequently weak correlation with relative humidity is due to the presence of the stratus cloud, which prevents radiative cooling at the surface (Román-Cascón *et al.*, 2019). For this reason, the temperature decrease during CBL fog formation is not as pronounced as in the observed radiation fog cases.

3.2.5 | CBL fog occurrence

Around 0500 on the third day, the cloud base reaches the ground again and CBL fog is detected, which persists for five hours. As in Román-Cascón *et al.* (2019), the CBL fog event forms after the descending of the base of a cloud that was previously radiation fog. The air temperature, relative humidity, and wind speed remain relatively constant. The visibility fluctuates between 1000 and 2000 m, remaining above the 1000-m visibility threshold. Compared with the previous radiation fog maturity, the visibilities during the presence of CBL fog are distinctly higher. The CBL fog layer is, on average, more elevated than the radiation fog layer, with a mean CBH of $11.68\,m$ for the CBL fog, while the CBH of radiation fog is $5.29\,m$. Visibilities below 1000 m measured at $2\,m$ agl indicate that the radiation fog layer begins at elevations below the CBH reported by the ceilometer. However, since the ceilometer has a minimum range of $5\,m$, as specified by the manufacturer (Lufft, 2025), measured CBH values below this range are not expected, but the actual CBH might be lower. In contrast, the mean CBH of the CBL fog layer is supported by high visibility readings (above 1000 m). As the visibility measurement is positioned at $2\,m$ agl, it measures the visibility below the cloud layer and therefore might not reflect the visibility of the CBL fog layer accurately. Consequently, additional visibility, temperature, and relative

humidity measurements at different heights are necessary for a more accurate estimate and description of the CBL processes.

3.2.6 | Cloud dissipation

The cloud base lifts again at 1000, which is faster than the cloud-base lowering, indicating the start of fog dissipation. From the backscatter intensity and CBH, it can be assumed that dissipation ends at 1400. The visibility increases again, inversely correlated with the relative humidity. The temperature also increases slowly and the wind speed oscillates between ≈ 1.0 and $2.5 \, \text{m} \cdot \text{s}^{-1}$. In general, the CBL fog event has less pronounced temperature changes and more variable wind speeds during the whole duration compared with the radiation fog event in case study 1 and the radiation fog event at the beginning of case study 2.

3.3 | Satellite-based life-cycle times compared with the visibility-based detected phases

In case study 1, the satellite-based FLS formation is indicated at 0400, two hours after the beginning of the visibility-based maturity phase, and the dissipation at 0815, 45 min before the start of the visibility-based dissipation phase. Between FLS formation and dissipation times, the fog layer reaches its maximum vertical extent. In this event, the satellite detects fog during the formation phase, indicated by two peaks of FLS occurrence. The first occurs at 2215 and the second at 0145, where a strong backscatter signal up to approximately 50 m agl is observed. The satellite-based formation time is later than the visibility-based formation time, shortly before the fog layer reaches its maximum vertical extent, as the fog is then dense enough to be detected by the satellite. In contrast, the satellite-based dissipation time is earlier than the visibility-based dissipation time, as the satellite is not able to detect FLS in twilight conditions (Egli *et al.*, 2017), leading to a shift in the dissipation time to earlier times (Pauli *et al.*, 2022a).

In case study 2, FLS formation is detected at 2130, 30 minutes after the beginning of the visibility-based maturity phase. Since FLS data do not discriminate between fog and low stratus (Cermak, 2018; Cermak & Bendix, 2011; Egli *et al.*, 2017), the dissipation of the radiation fog event and the formation of the CBL fog event are not detected by the satellite-based life-cycle detection method. Therefore, only one connected FLS event is observed, with a satellite-based dissipation time at 0400 on the third day of

the event. Similarly to case study one, the early dissipation is likely due to the twilight conditions, leading to "no-FLS" instances around sunrise and consequently the detection of a dissipation time in the logistic regression approach in Pauli *et al.* (2022a).

During the maturity phase, the backscatter signal shows the highest values and the satellite-based FLS mask shows mostly FLS presence. Developed, mature fog layers are denser and thus have more small droplets that reflect in the middle infrared, sending a stronger signal to the satellite than less developed fog masses. This property is used in the SOFOS algorithm (Cermak, 2006; Cermak & Bendix, 2007, 2008; Egli *et al.*, 2017), where the small-droplet proxy test distinguishes small-droplet clouds (e.g., FLS) from large-droplet clouds, assessing the radiative properties of FLS in the middle infrared (3.9 μm). At these wavelengths, small droplets are reflective and can be distinguished in the signal received by the satellite (Egli *et al.*, 2017). Therefore, the detectability of FLS from the satellite perspective is likely a function of the life-cycle stage of the FLS layer, where more developed fog layers are more easily detected than less dense or less developed ones (i.e., during the formation phase). We can, therefore, conclude that the visibility-based approach provides more accurate measures of formation and dissipation time at this location compared with the satellite-based approach, while the latter provides an approximate measure of FLS formation and dissipation time across large spatial scales, detecting fog at the maturity phase.

3.4 | Evaluation of the life-cycle phase detection method

Our results show that the visibility trend threshold for detecting the start of formation captures the beginning of the processes involved. From the ceilometer perspective, backscatter signals are stronger than those of clear sky but weaker than fog in the formation or mature phases. While these signals can be challenging to detect from the satellite perspective, the radiation fog in case study 1 is partly detected during the formation phase, which coincides with stronger backscatter signals in the ceilometer profile. The life-cycle phase detection method is not able to detect the formation phase when visibilities stay above the 1000-m fog threshold, which is the case for the CBL fog event in case study 2. A potential solution could be to use the patterns of relative humidity and cloud-base height in combination with the visibility threshold to be able to classify the formation phase of CBL events as well.

Formation and dissipation phases driven by stratus lowering and lifting can not be detected fully with the

visibility sensors at 2 m agl, as the cloud masses, where visibility changes are occurring, are located above the sensor. Therefore, the visibility thresholds at 2 m agl are ideal for the detection of radiation fog formation and dissipation but challenging for the detection of the life-cycle phases of CBL fog. A potential way to go forward would be to use visibility measurements at multiple heights, as shown recently in Parde *et al.* (2024). This could be used in future studies to detect the start of the formation phase or the end of the dissipation phase of fog events with stratus lowering or lifting processes involved.

The visibility thresholds for the detection of the dissipation phase show overall good agreement with the ceilometer profiles, the FLS mask, and the CBH. During dissipation, the backscatter reduces its intensity until no fog is observed at the end of the phase. This transition occurs faster compared with the formation phase, and the signal may change abruptly from one time step to the next. Additionally, a general change in the trend of visibility, temperature, relative humidity, and CBH is observed.

It has been shown that the three phases can be detected using visibility values and trends and that the ceilometer and satellite observations are useful in understanding the development of each phase. From the ceilometer perspective, changes in backscatter strength and CBH can give an approximate detection of the phases. These are, moreover, necessary to detect dissipation caused by stratus lifting or formation due to stratus lowering, which cannot be achieved by assessing visibility measurements at 2 m agl. Given the differences noted between radiation and CBL fog events, each fog type should be considered separately, deriving specific thresholds for each and preferring different data sources. For example, while radiation fog forms in the air layer above the ground, CBL fog forms from the lowering of the base of a stratus cloud to the surface. Therefore, visibility measurements at 2 m agl are suitable for assessing radiation fog formation, while visibility measurements at higher elevations (e.g., 100–200 m agl), along with ceilometer backscatter and CBH, are more suitable for assessing CBL fog formation. Additionally, a larger sample of fog events is required. The thresholds presented for the detection of radiation fog life-cycle phases should also be evaluated before applying the algorithm to other locations or other seasons. However, changes in threshold values should be small, since values from general definitions were implemented.

4 | CONCLUSIONS

In this study, we detected and characterized the life-cycle phases, namely formation, maturity, and dissipation, of

radiation fog events in autumn at the DWD station in Rheinstetten, Southwest Germany. FLS events at the study site were classified into fog or low stratus, and later the fog events into fog types (i.e., radiation and CBL fog), by combining satellite FLS data with ground-based observations of meteorological surface conditions and ceilometer backscatter. The phases of the radiation fog events were detected effectively based on station visibility observations, as well as their trend and two visibility thresholds. The algorithm developed provided a clear definition of the beginning and end of each phase based on the formation and dissipation processes involved that promote visibility changes. The algorithm also has the potential to run over long visibility time series to detect fog life-cycle phases automatically at different study sites.

The backscatter signals, the satellite FLS mask, and the CBH supported the phase detection. The phases detected showed evident patterns in visibility, temperature, relative humidity, and wind speed. Formation was characterized by increasing relative humidity and decreasing visibility, temperature, and wind speed; maturity by relatively constant values; and dissipation by inverse changes compared with those during formation, generally occurring faster than during formation. In general, the satellite FLS mask and backscatter profiles agreed in most cases, while the ceilometer detected fog presence earlier and more consistently and could also identify formation by stratus lowering or dissipation by stratus lifting. It was also shown that the satellite-based method detects the maturity phase, as defined in this study, consistently. As it was only possible to detect the life-cycle phases of the CBL fog event visually by observing the backscatter signal and CBH, the detection algorithm presented in this study should be improved in future studies by including CBH in the algorithm and evaluating more CBL events. The results show that the life-cycle classification scheme needs to be designed specific to the fog type, due to differences in the formation mechanisms of each one. For a better spatial characterization of fog life cycles, studies similar to those in this article are still required in other stations of the region, and the inclusion of more events would provide significant statistics, such as mean surface-condition parameters in each life-cycle phase.

In this study, a satellite-based life-cycle classification method was compared with a ground-based method for the first time, discussing the advantages and disadvantages of using each method and how the combination of both observation perspectives provides us with a better understanding of the fog life cycles. The findings of this article will provide a basis for future analysis of fog life cycles in the region with the aim of more accurate phase detection, as well as more exhaustive phase characterizations. These are needed for better predictions of fog formation

and dissipation for air, road, and marine transport management or the detection of climate-change-driven trends and shifts in the fog life cycle. The results of this study additionally outline the need for 24-hour consistent FLS datasets (Jahani *et al.*, 2025) and research efforts that are able to separate fog from low stratus clouds in satellite-based fog life-cycle studies. Finally, we propose that future satellite-based FLS detection methods include an assessment of the changes in the spectral signals of FLS during its life cycle, enabling a robust fog life-cycle phase detection from the satellite perspective.

ACKNOWLEDGEMENTS

CONFLICT OF INTEREST STATEMENT
The authors declare that they have no known competing financial interests or personal relationships that could have appeared to influence the work reported in this article.

DATA AVAILABILITY STATEMENT
The FLS occurrence mask dataset is available at the Laboratory of Climatology and Remote Sensing of the Phillips-University of Marburg: http://www.lcrs.de/data_pre.do?citid=291, and the FLS formation and dissipation dataset at the Repository KITopen of the Karlsruhe Institute of Technology: https://doi.org/10.5445/IR/1000141293 (both accessed February 1, 2024). Climate data of the German Weather Service are available at their Climate Data Center: https://opendata.dwd.de/climate_environment/CDC/ (accessed November 18, 2024). The ceilometer data from the German Weather Service are not available online and were requested for download. The datasets from Hijmans et al. (2005) are open-source and can be accessed from: http://www.worldclim.org.

ORCID
Maria Laura Pinilla https://orcid.org/0009-0006-2025-7382
Eva Pauli https://orcid.org/0000-0002-5506-4736
Johannes Antenor Senn https://orcid.org/0000-0001-6627-2568
Jan Cermak https://orcid.org/0000-0002-4240-595X

REFERENCES
American Meteorological Society. (2024) Fog. In: *Glossary of meteorology*. Available from: https://glossary.ametsoc.org/wiki/Fog

Bendix, J. (2002) A satellite-based climatology of fog and low-level stratus in Germany and adjacent areas [2nd International Conference on Fog and Fog Collection]. *Atmospheric Research*, 64(1), 3–18. Available from: https://doi.org/10.1016/S0169-8095(02)00075-3

Cermak, J. (2006) *SOFOS: a new satellite-based operational fog observation scheme*. PhD thesis, Philipps-Universität Marburg, Germany.

Cermak, J. (2018) Fog and low cloud frequency and properties from active-sensor satellite data. *Remote Sensing*, 10(8), 1209. Available from: https://doi.org/10.3390/rs10081209

Cermak, J. & Bendix, J. (2007) Dynamical nighttime fog/low stratus detection based on Meteosat SEVIRI data: a feasibility study. *Pure and Applied Geophysics*, 164, 1179–1192. Available from: https://doi.org/10.1007/s00024-007-0213-8

Cermak, J. & Bendix, J. (2008) A novel approach to fog/low stratus detection using Meteosat 8 data. *Atmospheric Research*, 87(3–4), 279–292. Available from: https://doi.org/10.1016/j.atmosres.2007.11.009

Cermak, J. & Bendix, J. (2011) Detecting ground fog from space – a microphysics-based approach. *International Journal of Remote Sensing*, 32(12), 3345–3371. Available from: https://doi.org/10.1080/01431161003747505

Cotton, W.R., Bryan, G. & van den Heever, S.C. (2011) Fogs and stratocumulus clouds. In: *International geophysics*, Vol. 99. Academic Press, pp. 179–485. Available from: https://doi.org/10.1016/S0074-6142(10)09912-2

Deutscher Wetter Dienst. (2021) DWD - Ceilometer data and trajectories. [Accessed 29th August 2024] https://www.dwd.de/EN/research/projects/ceilomap/ceilomap_node.html

Dione, C., Haeffelin, M., Burnet, F., Lac, C., Canut, G., Delanoë, J. et al. (2023) Role of thermodynamic and turbulence processes on the fog life cycle during SOFOG3D experiment. *Atmospheric Chemistry and Physics*, 23(24), 15711–15731. Available from: https://doi.org/10.5194/acp-23-15711-2023

Dupont, J.-C., Haeffelin, M., Protat, A., Bouniol, D., Boyouk, N. & Morille, Y. (2012) Stratus–fog formation and dissipation: A 6-day case study. *Boundary-Layer Meteorology*, 143, 207–225. Available from: https://doi.org/10.1007/s10546-012-9699-4

Dupont, J.-C., Haeffelin, M., Stolaki, S. & Elias, T. (2016) Analysis of dynamical and thermal processes driving fog and quasi-fog life cycles using the 2010–2013 ParisFog dataset. *Pure and Applied Geophysics*, 173(4), 1337–1358. Available from: https://doi.org/10.1007/s00024-015-1159-x

Egli, S., Thies, B., Drönner, J., Cermak, J. & Bendix, J. (2017) A 10 year fog and low stratus climatology for Europe based on meteosat second generation data. *Quarterly Journal of the Royal Meteorological Society*, 143(702), 530–541. Available from: https://doi.org/10.1002/qj.2941

Gottlieb, T.R., Eckardt, F.D., Venter, Z.S. & Cramer, M.D. (2019) The contribution of fog to water and nutrient supply to Arthraerua Leubnitziae in the central Namib desert, Namibia. *Journal of Arid Environments*, 161, 35–46. Available from: https://doi.org/10.1016/j.jaridenv.2018.11.002

Guerreiro, P.M., Soares, P.M., Cardoso, R.M. & Ramos, A.M. (2020) An analysis of fog in the mainland Portuguese international airports. *Atmosphere*, 11(11), 1239. Available from: https://doi.org/10.3390/atmos11111239

Gultepe, I., Tardif, R., Michaelides, S.C., Cermak, J., Bott, A., Bendix, J. et al. (2007) Fog research: a review of past achievements and

future perspectives. *Pure and Applied Geophysics*, 164, 1121–1159. Available from: https://doi.org/10.1007/s00024-007-0211-x

Hijmans, R.J., Cameron, S.E., Parra, J.L., Jones, P.G. & Jarvis, A. (2005) Very high resolution interpolated climate surfaces for global land areas. *International Journal of Climatology: A Journal of the Royal Meteorological Society*, 25(15), 1965–1978. Available from: https://doi.org/10.1002/joc.1276

Jahani, B., Karalus, S., Fuchs, J., Zech, T., Zara, M. & Cermak, J. (2025) Algorithm for continual monitoring of fog based on geostationary satellite imagery. *Atmospheric Measurement Techniques*, 18(8), 1927–1941. Available from: https://doi.org/10.5194/amt-18-1927-2025

Köhler, C., Steiner, A., Saint-Drenan, Y.-M., Ernst, D., Bergmann-Dick, A., Zirkelbach, M. et al. (2017) Critical weather situations for renewable energies–Part B: low stratus risk for solar power. *Renewable Energy*, 101, 794–803. Available from: https://doi.org/10.1016/j.renene.2016.09.002

Lamb, D. & Verlinde, J. (2011) *Physics and chemistry of clouds*. Cambridge, UK: Cambridge University Press.

Lufft. (2025) Technical Data Ceilometer CHM 15k NIMBUS, [Accessed 23th January 2025]. https://www.lufft.com/products/cloud-height-snow-depth-sensors-288/ceilometer-chm-15k-nimbus-2300/productAction/outputAsPdf/

Maalick, Z., Kühn, T., Korhonen, H., Kokkola, H., Laaksonen, A. & Romakkaniemi, S. (2016) Effect of aerosol concentration and absorbing aerosol on the radiation fog life cycle. *Atmospheric Environment*, 133, 26–33. Available from: https://doi.org/10.1016/j.atmosenv.2016.03.018

Maier, F., Bendix, J. & Thies, B. (2013) Development and application of a method for the objective differentiation of fog life cycle phases. *Tellus B: Chemical and Physical Meteorology*, 65(1), 19971. Available from: https://doi.org/10.3402/tellusb.v65i0.19971

Mattis, I. & Wagner, F. (2014) E-PROFILE: glossary of Lidar and ceilometer variables. [Accessed 29th August 2024] https://www.eumetnet.eu/wp-content/uploads/2016/10/ALC_glossary_revised_20140314.pdf

Mazoyer, M., Burnet, F. & Denjean, C. (2022) Experimental study on the evolution of droplet size distribution during the fog life cycle. *Atmospheric Chemistry and Physics*, 22(17), 11305–11321. Available from: https://doi.org/10.5194/acp-22-11305-2022

Mitchell, D., Henschel, J.R., Hetem, R.S., Wassenaar, T.D., Strauss, W.M., Hanrahan, S.A. et al. (2020) Fog and fauna of the Namib desert: past and future. *Ecosphere*, 11(1), e02996. Available from: https://doi.org/10.1002/ecs2.2996

Nakanishi, M. (2000) Large-eddy simulation of radiation fog. *Boundary-Layer Meteorology*, 94, 461–493. Available from: https://doi.org/10.1023/A:1002490423389

Parde, A.N., Ghude, S.D., Dhangar, N.G., Bhautmage, U.P., Wagh, S., Lonkar, P. et al. (2024) Challenges in simulating prevailing fog types over urban region of Delhi. *Journal of Geophysical Research: Atmospher5e34s*, 129(7), e2023JD039772. Available from: https://doi.org/10.1029/2023JD039772

Pauli, E., Andersen, H., Bendix, J., Cermak, J. & Egli, S. (2020) Determinants of fog and low stratus occurrence in continental central Europe – a quantitative satellite-based evaluation. *Journal of Hydrology*, 591, 125451. Available from: https://doi.org/10.1016/j.jhydrol.2020.125451

Pauli, E., Cermak, J. & Andersen, H. (2022a) A satellite-based climatology of fog and low stratus formation and dissipation times in central Europe. *Quarterly Journal of the Royal Meteorological Society*, 148(744), 1439–1454. Available from: https://doi.org/10.1002/qj.4272

Pauli, E., Cermak, J., Andersen, H. & Fuchs, J. (2024a) An analysis of fog and low stratus life-cycle regimes over central Europe. *Quarterly Journal of the Royal Meteorological Society*, 150(761), 2382–2396. Available from: https://doi.org/10.1002/qj.4714

Pauli, E., Cermak, J., Bendix, J. & Stier, P. (2024b) Synoptic scale controls and aerosol effects on fog and low stratus life cycle processes in the Po valley Italy. *Geophysical Research Letters*, 51(20), e2024GL111490. Available from: https://doi.org/10.1029/2024GL111490

Pauli, E., Cermak, J. & Teuling, A.J. (2022b) Enhanced nighttime fog and low stratus occurrence over the Landes forest, France. *Geophysical Research Letters*, 49, e2021GL097058. Available from: https://doi.org/10.1029/2021GL097058

Pérez-Díaz, J.L., Ivanov, O., Peshev, Z., Álvarez-Valenzuela, M.A., Valiente-Blanco, I., Evgenieva, T. et al. (2017) Fogs: Physical basis, characteristic properties, and impacts on the environment and human health. *Water (Basel)*, 9(10), 807. Available from: https://doi.org/10.3390/w9100807

Price, J. (2011) Radiation fog. Part I: observations of stability and drop size distributions. *Boundary-Layer Meteorology*, 139, 167–191. Available from: https://doi.org/10.1007/s10546-010-9580-2

Price, J. (2019) On the formation and development of radiation fog: an observational study. *Boundary-Layer Meteorology*, 172(2), 167–197. Available from: https://doi.org/10.1007/s10546-019-00444-5

Qiao, N., Wang, L., Marais, E. & Li, F. (2022) Fog detection and estimation using CALIPSO Lidar observations. *Geophysical Research5L55etters*, 49(24), e2022GL101375. Available from: https://doi.org/10.1029/2022GL101375

Román-Cascón, C., Yagüe, C., Steeneveld, G.-J., Morales, G., Arrillaga, J.A., Sastre, M. et al. (2019) Radiation and cloud-base lowering fog events: observational analysis and evaluation of WRF and HARMONIE. *Atmospheric Research*, 229, 190–207. Available from: https://doi.org/10.1016/j.atmosres.2019.06.018

Seely, M. (1979) Irregular fog as a water source for desert dune beetles. *Oecologia*, 42(2), 213–227. Available from: https://doi.org/10.1007/BF00344858

Smith, D., Renfrew, I., Price, J. & Dorling, S. (2018) Numerical modelling of the evolution of the boundary layer during a radiation fog event. *Weather*, 73(10), 310–316. Available from: https://doi.org/10.1002/wea.3305

Smith, D.K., Dorling, S.R., Renfrew, I.A., Ross, A.N. & Poku, C. (2023) Fog trends in India: relationships to fog type and western disturbances. *International Journal of Climatology*, 43(2), 818–836. Available from: https://doi.org/10.1002/joc.7832

Tardif, R. & Rasmussen, R.M. (2007) Event-based climatology and typology of fog in the New York City region. *Journal of Applied Meteorology and Climatology*, 46(8), 1141–1168. Available from: https://doi.org/10.1175/JAM2516.1

Toledo, F., Haeffelin, M., Wærsted, E. & Dupont, J.-C. (2021) A new conceptual model for adiabatic fog. *Atmospheric Chemistry and Physics*, 21(17), 13099–13117. Available from: https://doi.org/10.5194/acp-21-13099-2021

Vautard, R., Yiou, P. & Van Oldenborgh, G.J. (2009) Decline of fog, mist and haze in Europe over the past 30 years. *Nature Geoscience*, 2(2), 115–119. Available from: https://doi.org/10.1038/ngeo414

Wærsted, E.G., Haeffelin, M., Steeneveld, G.-J. & Dupont, J.-C. (2019) Understanding the dissipation of continental fog by analysing the LWP budget using idealized les and in situ observations. *Quarterly Journal of the Royal Meteorological Society*, 145(719), 784–804. Available from: https://doi.org/10.1002/qj.3465

Wang, L., Kaseke, K.F., Ravi, S., Jiao, W., Mushi, R., Shuuya, T. et al. (2019) Convergent vegetation fog and dew water use in the Namib Desert. *Ecohydrology*, 12(7), e2130. Available from: https://doi.org/10.1002/eco.2130

Warren-Rhodes, K.A., McKay, C.P., Boyle, L.N., Wing, M.R., Kiekebusch, E.M., Cowan, D.A. et al. (2013) Physical ecology of hypolithic communities in the central Namib Desert: the role of fog, rain, rock habitat, and light. *Journal of Geophysical Research: Biogeosciences*, 118(4), 1451–1460. Available from: https://doi.org/10.1002/jgrg.20117

Weston, M., Francis, D., Nelli, N., Fonseca, R., Temimi, M. & Addad, Y. (2022) The first characterization of fog microphysics in the United Arab Emirates, an arid region on the Arabian Peninsula. *Earth and Space Science*, 9(2), e2021EA002032. Available from: https://doi.org/10.1029/2021EA002032

World Meteorological Organization. (2017) Fog. In: *International cloud atlas*. Available from: https://cloudatlas.wmo.int/en/fog.html

SUPPORTING INFORMATION

Additional supporting information can be found online in the Supporting Information section at the end of this article.

How to cite this article: Pinilla, M.L., Pauli, E., Senn, J.A. & Cermak, J. (2025) Classification of Fog Life-Cycle Phases Using Ground-Based and Satellite-Based Observations. *Quarterly Journal of the Royal Meteorological Society*, e70056. Available from: https://doi.org/10.1002/qj.70056